



Rationalization of solidification mechanism of Nd–Fe–B magnets during laser directed-energy deposition

Niyanth Sridharan^{1,2}, Ercan Cakmak³, Fred A. List², Huseyin Ucar^{4,7}, Steve Constantinides^{5,8}, S. S. Babu^{1,2}, S. K. McCall⁶, and M. Parans Paranthaman^{4,*}

¹Department of Mechanical Aerospace Bio Medical Engineering, University of Tennessee, Knoxville, TN 37996, USA

²Manufacturing Demonstration Facility, Material Science and Technology Division, Oak Ridge National Laboratory, Oak Ridge, TN 37831, USA

³Material Science and Technology Division, Oak Ridge National Laboratory, Oak Ridge, TN 37831, USA

⁴Chemical Sciences Division, Oak Ridge National Laboratory, Oak Ridge, TN 37831, USA

⁵Arnold Magnetic Technologies Corp, Rochester, NY 14625, USA

⁶Lawrence Livermore National Laboratory, Livermore, CA 94550, USA

⁷Present address: Florida Polytechnic University, Lakeland, USA

⁸Present address: Magnetics & Materials LLC, Honeoye, NY 14471, USA

Received: 13 November 2017

Accepted: 26 February 2018

Published online:

7 March 2018

© Springer Science+Business Media, LLC, part of Springer Nature (outside the USA) 2018

ABSTRACT

Near-net fabrication techniques are highly beneficial to minimize rare earth metal usage to fabricate dense fully functional magnets. In this study, feasibility of using the directed-energy deposition technique for fabrication of magnets is evaluated. The results show that despite the ability to fabricate highly reactive materials in the laser deposition process, the magnetic coercivity and remanence of the hard magnets is significantly reduced. X-ray powder diffraction in conjunction with electron microscopy showed that the material experienced a primary Nd₂Fe₁₇B_x solidification. Consequently, the absence of the hard magnetic phase resulted in deterioration of the build properties.

Notice: This manuscript has been authored by UT-Battelle, LLC under Contract No. DE-AC05-00OR22725 with the U.S. Department of Energy. The United States Government retains and the publisher, by accepting the article for publication, acknowledges that the United States Government retains a non-exclusive, paid-up, irrevocable, world-wide license to publish or reproduce the published form of this manuscript, or allow others to do so, for United States Government purposes. The Department of Energy will provide public access to these results of federally sponsored research in accordance with the DOE Public Access Plan (<http://energy.gov/downloads/doe-public-access-plan>)

Address correspondence to E-mail: paranthamanm@ornl.gov

<https://doi.org/10.1007/s10853-018-2178-7>

Introduction

Different types of rare earth magnets that show excellent magnetic properties are based on $\text{Nd}_2\text{Fe}_{14}\text{B}$, SmCo_5 , $\text{Sm}_2\text{Co}_{17}$ and $\text{Sm}_2\text{Fe}_{17}\text{N}_x$ alloys with a large magneto-crystalline anisotropy of the hard magnetic phase [1]. These high performance permanent magnets derive their magnetic properties from the high magneto-crystalline anisotropy field H_k provided by the interaction of the 3d–4f electrons in the rare earth and transition metals [2]. The addition of the rare earth constituents is crucial to the magnetic properties of these magnets. Recent developments have been made to enhance coercivity and reduce material costs by minimizing the heavy rare earth element (HREE) addition to these magnets [3]. Rare earth-based permanent magnets are the key components in environmentally friendly technologies such as electric transportation (automotive, marine and aerospace) and direct or hybrid drive wind turbines. Rare earth permanent magnets remain a critical part of data storage [2]. However, the high cost of rare earth raw materials and issues related to an adequate and dependable supply of heavy rare earths, e.g., dysprosium, are holding back the adoption or expanded use of these technologies.

Nd–Fe–B-based permanent magnets were initially reported in late 1981 [4, 5], and ever since significant strides have been made in the development of new fabrication techniques [6]. They exhibit at least three equilibrium phases, i.e., $\text{Nd}_2\text{Fe}_{14}\text{B}$ Φ phase, the hard magnetic phase and the low melting Nd-rich phase (η) [3]. A multi-step process has traditionally been used to fabricate these magnets [7]. NdFeB is cast into ingots, after casting it is pulverized with a coarse grind, and then it is jet milled. The resulting particle size is between 3 and 4 μm (Fisher Sub-Sieve Sizer, FSSS). Following this, the anisotropic powder is aligned in a magnetic field of between 10 and 20 kOe and pressed into a partially dense compact [7]. The compacts are sintered at 1070 °C and cooled rapidly. Following the high-temperature sintering, the material is given another thermal treatment at 600 °C to promote grain refinement and relieve mechanical stress [7].

Advances in strip casting of rare earth alloys during the mid- to late 1990s have resulted in a refined microstructure in cooling from the melt resulting in less alpha iron phase segregation and improved

2:14:1 crystal development. The high cooling rate results in a fine grain structure and permitting a lower rare earth content closer to stoichiometric [8, 9]. Fully dense NdFeB-type materials are brittle, and hence, machining can be expensive. Machining also leads to significant material waste up to 50% and longer manufacturing times. Considering the growing shortage of critical rare earth metals, it is important to explore alternate, near-net shape manufacturing techniques to reduce the material waste and the costs associated with secondary processing.

Additive manufacturing (AM) is a near-net shape manufacturing technique, which can produce final parts with minimal material waste [10]. Several AM techniques are available and are broadly classified based on the nature of the process as *powder bed* and *powder blown* [11]. We have recently demonstrated the successful fabrication of NdFeB bonded magnets using the material extrusion and binder jetting additive manufacturing techniques [12, 13]. The 3D printed bonded magnets exhibit magnetic and mechanical properties comparable to those of injection molded products. Nevertheless, bonded magnets in general suffer from disadvantages such as reduced energy product due to the dilution of the magnetization by polymer binders. Exploiting printing metallic sintered magnet would be beneficial to the clean energy industry which depends heavily on strong sintered magnets.

In this work, a powder-blown directed-energy deposition technique has been used to fabricate NdFeB sintered magnet. This process is based on the coaxial laser cladding process where the part is built in layers. The primary process parameters used to control the deposit geometry and part density are the laser power, travel speed and powder feed rate. So far only limited feasibility studies have been attempted to fabricate magnets using additive manufacturing. Since the additive manufacturing process experiences naturally rapid cooling rates, the interface velocities and the solidification structure can be significantly different from those of the conventional manufacturing process. In addition, it has been shown that by increasing the solid–liquid interface velocities, it is possible to obtain the desired $\text{Nd}_2\text{Fe}_{14}\text{B}$ microstructure. Due to the rapid interface velocities in the laser DMD (direct metal deposition) processing, it is hypothesized to shift the solidification mode from non-magnetic or soft phase such as

primary γ iron to primary $\text{Nd}_2\text{Fe}_{14}\text{B}$, thereby maximizing the magnetic properties. Hence, the aim of this work is twofold:

1. Feasibility of fabricating NdFeB magnets using the laser powder-blown directed-energy deposition
2. Investigation of the solidification process occurring during laser processing of these builds with correlation of the microstructure with the magnetic properties

Experimental procedure

Commercial Magnequench anisotropic MQA-38-14 (designated as MQA) and isotropic spherical MQP-S-11-9 (designated as MQP) NdFeB powders were used for this study. It should be noted that spherical particles are preferred for laser additive process. MQA powders yield substantially higher-energy product and remanence compared to MQP powders. Fabrication was performed using the DM103D laser directed-energy system with a 1-kW high-power diode laser operating at a wavelength of 910 nm. The depositions were performed under an Argon blanket, where the oxygen content was < 5 ppm, to avoid oxidation of the rare earth metals. In addition to this, a stream of Argon was also delivered coaxially along with the powder to shield the melt pool from oxidation and contamination. The builds were fabricated using a laser power of 500 W, a powder feed rate of 5.3 g/min and a travel speed of 700 mm/min. A total of 25 layers were built, and the approximate build height was about 12.5 mm with a height of 0.5 mm/layer. To rationalize the observed magnetic properties, characterization was performed to measure the phase fractions in the build. Following fabrication of the builds, magnetization properties of the builds were measured using a Quantum Design MPMS-5 SQUID magnetometer. X-ray diffraction (XRD) was used to perform the phase identification and quantification measurements for both the as-built material and the as-received powder. A PANalytical X'Pert PRO diffractometer with $\text{Mo K}\alpha$ radiation ($\lambda = 0.709319 \text{ \AA}$) was used for these measurements. Phase identification was performed using the JADE software whereas quantification was achieved through Rietveld refinement using the HighScore Plus program. Sections were then prepared for

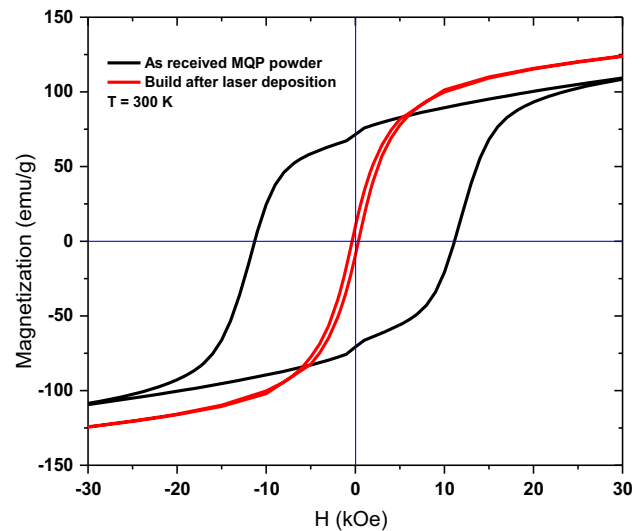


Figure 1 Magnetization curve of the powder and the sample. Note the sharp drop in coercivity and remanence of the magnets after processing.

metallographic analysis and polished using standard metallographic techniques. Microstructure analysis of the deposit was then performed using a JEOL 6500S SEM operated at an accelerating voltage of 20 kV. Microstructure analysis of the deposit was then performed using a JEOL 6500S SEM operated at an accelerating voltage of 20 kV.

Results and discussions

Figure 1 shows the hysteresis loops for both as-received MQP powders and build after laser deposition. The magnetization for build at 35 kOe reached about 127.2 emu/g, whereas the starting MQP powder with a theoretical density of 7.43 g/cm^3 reached only 113.0 emu/g. There is a small normal hysteresis of 500 Oe retained in this material, but the vast majority of the coercivity was lost after laser processing implying that hard magnetic phase did not survive. One initial hypothesis to rationalize the loss in properties was that the rare earth evaporated during the process. Follow-up chemical composition testing showed that this was not the case. The results from the composition analysis are presented in Table 1. Normally the formation of magnetic properties is associated with the formation of the tetragonal $\text{Nd}_2\text{Fe}_{14}\text{B}$ phase. The poor magnetic properties could be attributed to the absence of $\text{Nd}_2\text{Fe}_{14}\text{B}$ or the creation of alternate, possibly soft phases. The poor

Table 1 Chemical analysis of the magnets after laser direct deposition process

Element	O	C	Nd	Fe	B	Pr	Ni	Mo	Cr
Weight %	0.091	0.147	16.9	69.5	1.76	2.02	0.020	0.019	0.055

Values presented are weight percent. Very minor impurities of other metals are also present

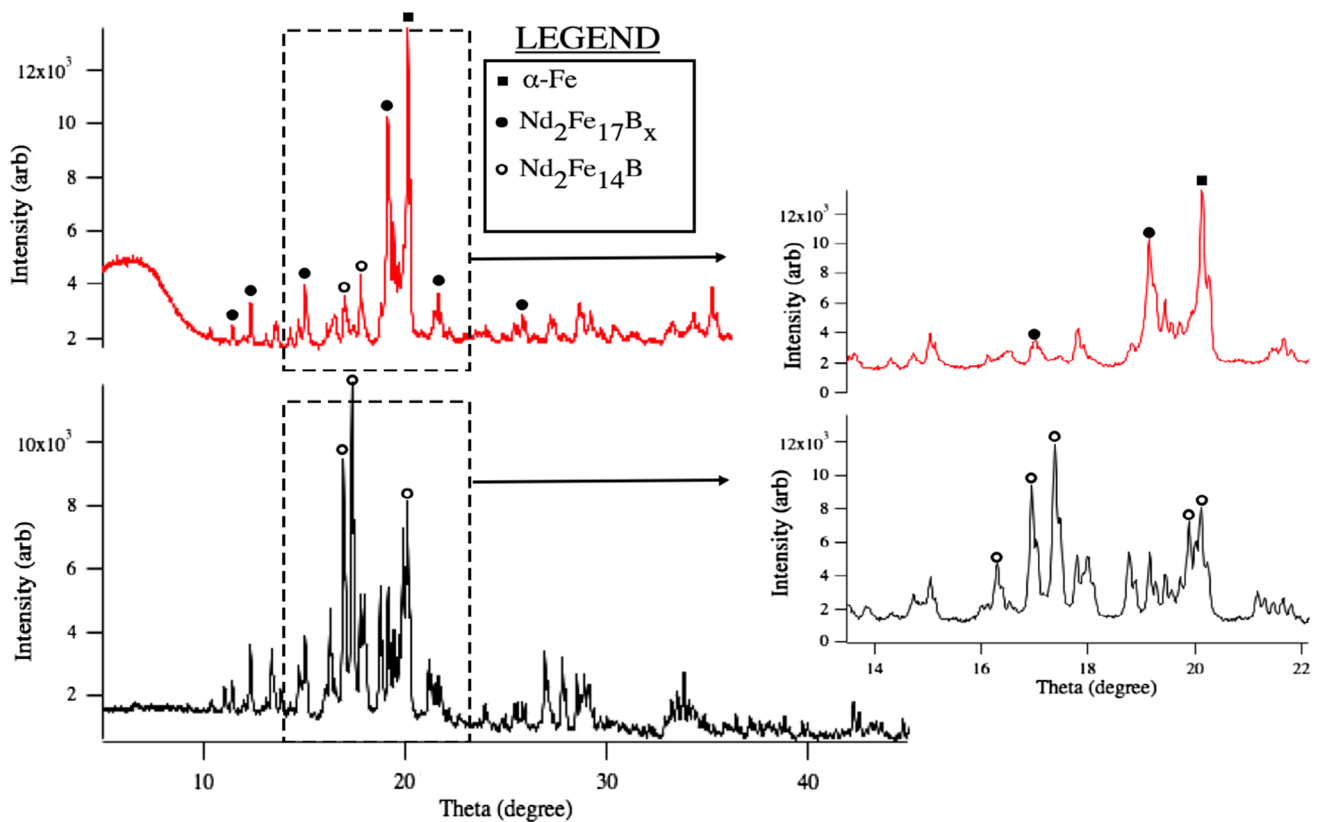


Figure 2 XRD patterns obtained from the powder (shown below in black) and the build (shown above in red). Note the sharp decrease in the intensity of the peaks corresponding to the

magnetic properties could be attributed to the absence of $\text{Nd}_2\text{Fe}_{14}\text{B}$. XRD patterns obtained from the as-received MQA powder and the as-built sample are shown in Fig. 2. Figure 2 shows that the as-received powder contained almost 100% $\text{Nd}_2\text{Fe}_{14}\text{B}$, while the as-built sample showed the presence of additional phases. Peaks belonging to $\text{Nd}_2\text{Fe}_{17}\text{B}_x$ and $\alpha\text{-Fe}$ phases were identified in addition to the $\text{Nd}_2\text{Fe}_{14}\text{B}$ phase. The lattice parameters of the constituent phases were obtained from the Rietveld refinements. Accordingly, the lattice parameter of alpha Fe was found to be $a = 2.8701 \text{ \AA}$, which is close to the literature value [14–20]. On the other hand, the lattice parameters of the $\text{Nd}_2\text{Fe}_{14}\text{B}$ phase were calculated to be $a = 8.7963 \text{ \AA}$, $c = 12.1923 \text{ \AA}$ and $a = 8.7974 \text{ \AA}$, $c = 12.1509 \text{ \AA}$ for the as-received powder and the as-built sample,

$\text{Nd}_2\text{Fe}_{14}\text{B}$ hard magnetic phase in the additively manufactured samples. Also note the corresponding increase in the intensity in the alpha iron peak after laser processing.

respectively. While the a-lattice parameter did not change much, the shift in the c-lattice parameter suggests that there may have been elemental composition change leading to the formation of a magnetically soft phase. To confirm the above hypothesis, a systematic multi-scale characterization needs to be performed. The observed lattice parameters from the as-built sample agree with those reported for $\text{Nd}_2\text{Fe}_{17}\text{B}_x$ [19]. The formation of secondary phases also leads to a diminishing of the desirable hard magnetic phase. The presence of alpha iron will shunt the field internally reducing H_{c_j} . To rationalize the drop-in properties, the solidification sequence in the material needs to be understood under non-equilibrium conditions. The composition of the metal stable phase was determined to be $x = 1$ in $\text{Nd}_2\text{Fe}_{17}\text{B}_x$ [21].

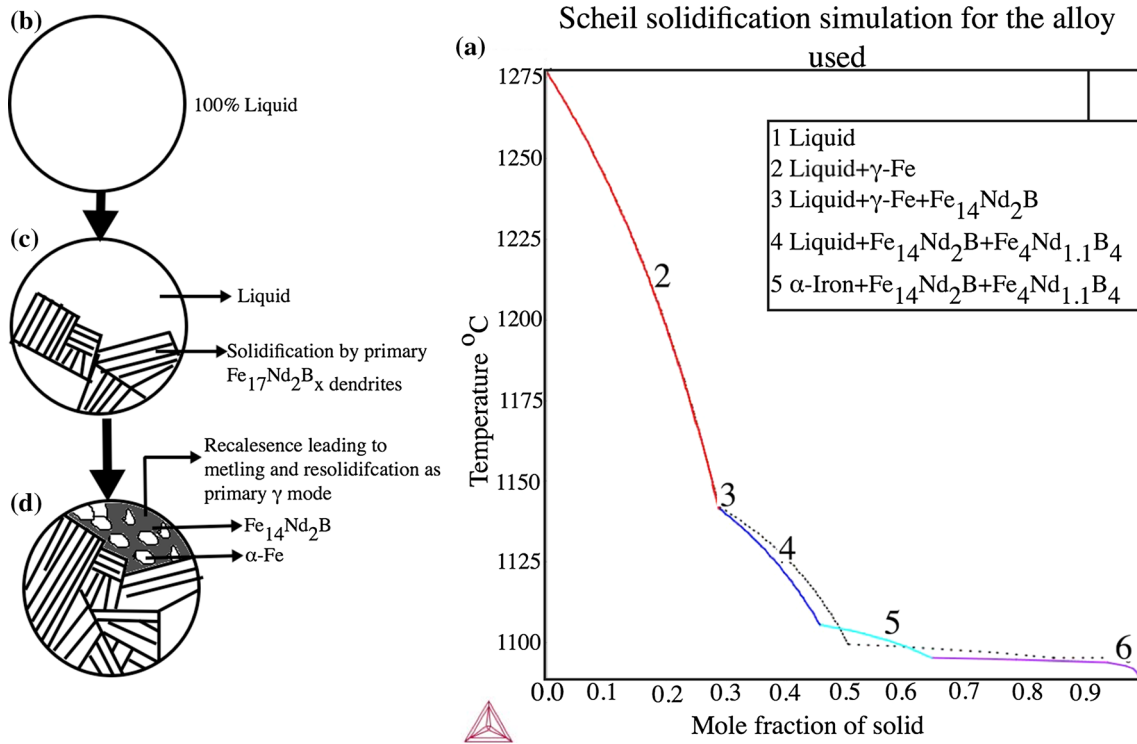
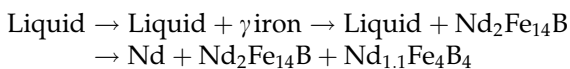


Figure 3 a Scheil–Gulliver solidification simulation and a schematic illustrating the solidification sequence; and b–d the schematic illustration of solidification sequence in the builds. $\text{Nd}_2\text{Fe}_{17}\text{B}_x$ nucleates in the melt and solidifies. However,

recalescence events lead to temperature excursions leading to local melting and re-solidification with the primary γ mode. The subsequent allotropic transformation of the primary γ to α leads to the observed microstructure shown in Fig. 3c.

Typically $\text{Nd}_2\text{Fe}_{14}\text{B}$ is expected to solidify by a primary γ iron mode and subsequently transform peritectically to $\text{Nd}_2\text{Fe}_{14}\text{B}$ by a $L + \gamma \rightarrow \text{Nd}_2\text{Fe}_{14}\text{B}$ reaction [22]. However, due to the rapid cooling rates encountered during the laser deposition process, the peritectic reaction can be suppressed which results in the absence of the $\text{Nd}_2\text{Fe}_{14}\text{B}$ in the build [14, 16, 19].

To understand the exact mechanism of solidification, Scheil–Gulliver solidification simulation was performed using THERMOCALC[®], a commercially available CALPHAD-based technique. The results are shown in Fig. 3. The equilibrium pseudo-binary phase diagram figure shows that for the compositions used currently solidification starts in the $L + \gamma$ iron region. Low solubility of Nd and B in the gamma phase results in the rejection of Nd and B in the melt, and progressively the remaining liquid becomes enriched in solute. The solidification sequence for the alloy under consideration as per the Scheil–Gulliver simulation is as follows:



However, the X-ray diffraction data show the presence of a metastable $\text{Nd}_2\text{Fe}_{17}\text{B}_x$ phase something that the Scheil solidification simulation does not predict. However, the solidification simulation does not consider the growth velocity of the solid liquid interfaces during solidification. Liquid/solid interface velocity becomes a significant factor governing the phase selection mechanism [23]. It has been shown using interface response functions that the solidification mode shifts from primary γ to primary $\text{Nd}_2\text{Fe}_{14}\text{B}$ when the interface velocity exceeds 10^{-3} m/s [24]. For a circular melt pool, the interface velocity is the welding speed at the center [25], which for this case is close to 11×10^{-3} m/s (700 mm/min). Hence, a shift in the solidification mode is quite possible. Gao et al. [14, 16, 18, 19] have shown that under conditions of a critical undercooling (~ 60 K), the nucleation of $\text{Nd}_2\text{Fe}_{17}\text{B}_x$ becomes favorable compared to $\text{Nd}_2\text{Fe}_{14}\text{B}$. Undercooling of the order of 60 K can occur under rapid solidification conditions such as additive manufacturing, and the shift in solidification mode to $\text{Nd}_2\text{Fe}_{17}\text{B}_x$ from $\text{Nd}_2\text{Fe}_{14}\text{B}$ or γ -Fe can occur [25]. This undercooling promotes the

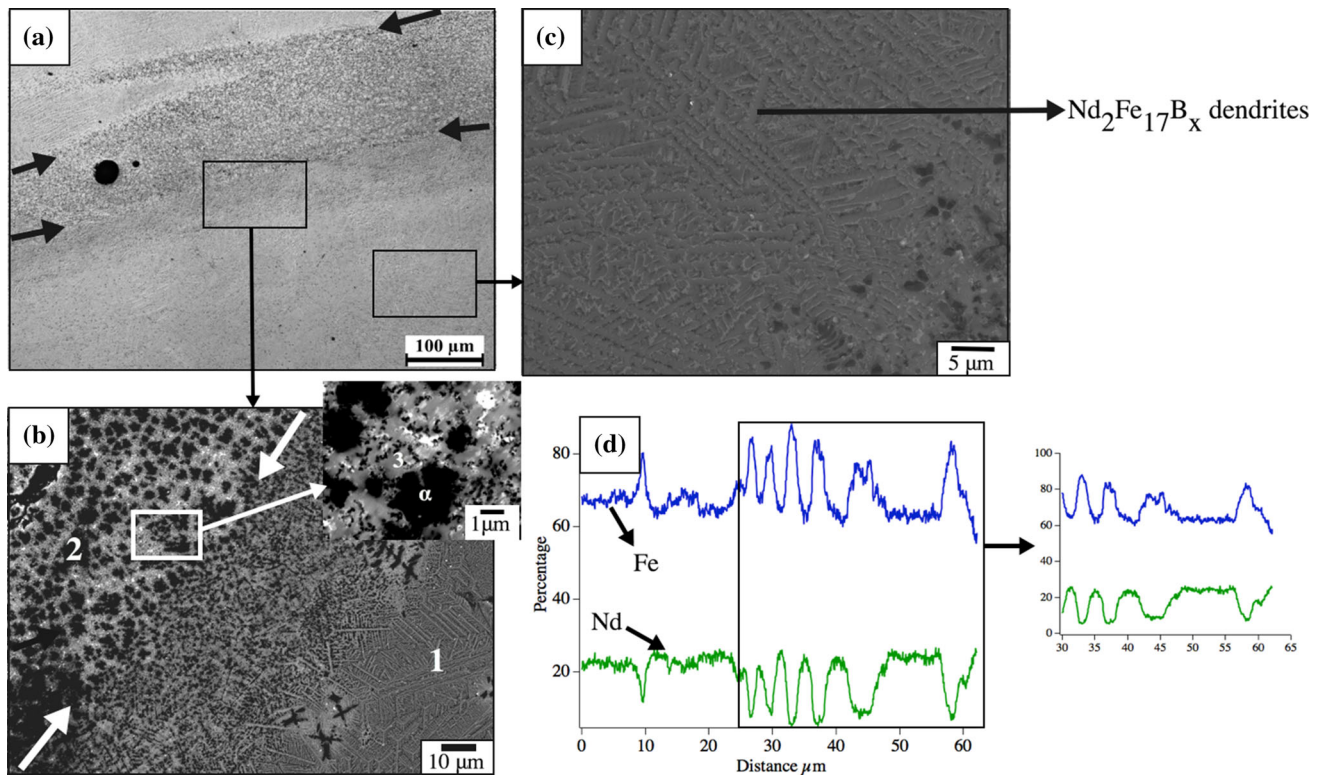


Figure 4 **a** Optical microscopy shows that solidification did proceed in two stages. The final stage to solidify is shown inside the arrows. Note that this zone is sandwiched between two zones, which solidified as $\text{Nd}_2\text{Fe}_{17}\text{B}_x$ showing that recoalescence events result in the solidification in the primary γ mode; **b** the zone marked using the arrows has dendritic alpha iron and $\text{Nd}_2\text{Fe}_{14}\text{B}$.

nucleation of the magnetically soft $\text{Nd}_2\text{Fe}_{17}\text{B}_x$ [14]. If the solidification occurred by a primary $\text{Nd}_2\text{Fe}_{17}\text{B}_x$, it does not explain the presence of $\text{Nd}_2\text{Fe}_{14}\text{B}$ and α -Fe in the final builds. Hence, to rationalize this, optical and SEM examination was performed, and the results are shown in Fig. 4.

Figure 4a clearly shows two “bands” (dark etching regions in the build) in the solidified structure. The bands are marked with arrows in Fig. 4a. These bands were present throughout the build at regular intervals. Surrounding the band are the $\text{Nd}_2\text{Fe}_{17}\text{B}_x$ dendrites characterized by the light etching structure. Electron microscopy results in Fig. 4b show that the bands exhibit a Nd-rich structure (the bright white spots) + alpha Fe dendrites (dark etching phases marked “ α ”) and “2” plus $\text{Nd}_2\text{Fe}_{14}\text{B}$ structures (the featureless gray regions marked by the “3”). The microstructure shown in Fig. 4b is the equilibrium microstructure that one would expect. The number of recoalescence events that the alloy undergoes during

The bright white regions shown in figure (b) correspond to Nd-rich phase. Note the fluctuation in the Nd and Fe in the region showing solute rejection near the primary gamma phase; c shows the structure of the primary $\text{Nd}_2\text{Fe}_{17}\text{B}_x$ dendrites; and d EDS spectra showing a compositional map of Nd and Fe in the build.

solidification may explain this apparent shift in solidification mode. During solidification in the primary $\text{Nd}_2\text{Fe}_{17}\text{B}_x$ mode, the material experiences a 150 K rise in temperature at 1400 K [14]. This temperature excursion causes the region to exceed the solidus temperature. As a result of this rise in temperature, the banded zone melts and re-solidifies. When it re-solidifies, it solidifies in the primary austenite mode and hence shows the microstructure that the Scheil solidification simulation predicts [14, 15]. In addition, EDS spectra reported in Fig. 4d show that solidification products in the re-melted region experience significant partitioning of alloying elements while the $\text{Nd}_2\text{Fe}_{17}\text{B}_x$ region does not show any detectable partitioning of Nd within the dendrites. This shows that the region in the bands experienced a much slower interface velocity leading to the solidification of a primary γ phase.

It is clear that to prevent the loss in the coercivity and remanence in the build it is necessary to retain

the $\text{Nd}_2\text{Fe}_{14}\text{B}$ phase. Hence, we need to engineer the solidification sequence so that the build solidifies as a primary $\text{Nd}_2\text{Fe}_{14}\text{B}$. Very recently, Jacimovic et al. [26] demonstrated the printing Nd-Fe-B magnets by selective laser melting of metals. They succeeded by fine-tuning the laser (pulsed Nd:YAG with a maximum energy output of 120 W LP) parameters such as speed, power and focus with the control of the thickness of the deposited powder layer. The high cooling rate and the composition of MQP-S alloy resulted in stabilization of the intended $\text{Nd}_2\text{Fe}_{14}\text{B}$ magnetic phase with small iron segregation compared to the slow cooling rate resulted in much higher amounts of iron.

Conclusions

In this work, we report the feasibility of using the directed-energy additive manufacturing technique to successfully handle reactive rare earth elements without any significant loss of alloying elements. Though builds were successfully fabricated, the magnetic properties were significantly reduced from that of the starting alloy. X-ray diffraction showed a large fraction of $\text{Nd}_2\text{Fe}_{17}\text{B}_x$ and some $\text{Nd}_2\text{Fe}_{14}\text{B}$ along with a significant fraction of α -Fe. Since this could not be explained by current theories, microscopy and CALPHAD-based techniques were used to rationalize the observed microstructure. The microstructure was a result of the primary $\text{Nd}_2\text{Fe}_{17}\text{B}_x$ solidification, promoted by a rapid liquid solid interface velocity ($> 10^{-3}$ m/s). Recalescence events during solidification resulted in remelting part of the $\text{Nd}_2\text{Fe}_{17}\text{B}_x$ leading to the solidification in the primary γ phase. This leads to the formation of the observed bands and causes the observed (α -Fe + $\text{Nd}_2\text{Fe}_{14}\text{B}$ + $\text{Nd}_2\text{Fe}_{17}\text{B}_x$) microstructure to form.

Acknowledgements

This research (HU, MPP, SKM) was supported by the Critical Materials Institute, an Energy Innovation Hub funded by the US Department of Energy, Office of Energy Efficiency and Renewable Energy, Advanced Manufacturing Office. Work at LLNL under Contract DE-AC52-07NA27344. Part of this research was also supported by the US Department of Energy, Office of Energy Efficiency and Renewable

Energy, Manufacturing Demonstration Facility Tech Proposal with Arnold Magnetic Technologies. Thanks are due to Jim Herchenroeder at Molycorp Magnequench for providing magnet powders for this study. Thanks are also due to Dr. Ling Li for valuable discussions.

References

- [1] Stadelmaier H (1990) *J Mater Eng* 12:185
- [2] Lewis LH, Jiménez-Villacorta F (2013) *Metall Mater Trans A* 44:2
- [3] Fidler J, Schrefl T (1996) *J Appl Phys* 79:5029
- [4] Croat JJ, Herbst JF, Lee RW, Pinkerton FE (1984) *J Appl Phys* 55:2078
- [5] Sagawa M, Fujimura S, Togawa N, Yamamoto H, Matsuura Y (1984) *J Appl Phys* 55:2083
- [6] Ma B, Herchenroeder J, Smith B, Suda M, Brown D, Chen Z (2002) *J Magn Magn Mater* 239:418
- [7] Brown D, Ma B-M, Chen Z (2002) *J Magn Magn Mater* 248:432
- [8] Hirose Y, Hasegawa H, Sasaki S, Sagawa M (1998) In: *Proceedings of 15th International Workshop on REPM and Their Applications*, Dresden, Germany
- [9] Sasaki S, Hasegawa H, Hirose Y (1999) Google patents
- [10] Gibson I, Rosen DW, Stucker B (2010) *Additive manufacturing technologies*. Springer, New York
- [11] Gu D, Meiners W, Wissenbach K, Poprawe R (2012) *Int Mater Rev* 57:133
- [12] Li L, Tirado A, Nlebedim IC et al (2016) *Sci Rep* 6:36212. <https://doi.org/10.1038/srep36212>
- [13] Li L, Post B, Kunc V, Elliott AM, Paranthaman MP (2017) *Scripta Mater*. <https://doi.org/10.1016/j.scriptamat.2016.12.035>
- [14] Gao J, Volkmann T, Herlach D (2002) *Acta Mater* 50:3003
- [15] Gao J, Volkmann T, Herlach D (2001) *J Mater Res* 16:2562
- [16] Gao J, Volkmann T, Roth S, Löser W, Herlach D (2001) *J Magn Magn Mater* 234:313
- [17] Gao J, Volkmann T, Yang S, Reutzel S, Herlach D, Song X (2007) *J Alloy Compd* 433:356
- [18] Li J, Liu Y, Gao S, Li M, Wang Y, Tu M (2006) *J Magn Magn Mater* 299:195
- [19] Volkmann T, Strohmenger J, Gao J, Herlach DM (2004) *Appl Phys Lett* 85:2232
- [20] Ozawa S, Kuribayashi K, Hirosawa S, Reutzel S, Herlach D (2006) *J Appl Phys* 100:123906
- [21] Schneider G, Henig ET, Petzow G, Stadelmaier HH (1987) *Z Metallkde* 77:755

- [22] Schneider G, Landgraf FJ, Missell FP (1989) *J Less Common Met* 153:169
- [23] Babu S (2009) *Int Mater Rev* 54:333
- [24] Umeda T, Okane T, Kurz W (1996) *Acta Mater* 44:4209
- [25] David S, Vitek J (1989) *Int Mater Rev* 34:213
- [26] Jacimovic J, Binda F, Herrmann LG, Greuter F, Genta J, Calvo M, Tomse T, Simon RA (2017) *Adv Eng Mater*. <https://doi.org/10.1002/adem.201700098>